Failure Effect Analysis and Reconfiguration of Thrusters Based on Inverse Simulation of Manually Controlled RVD

Wanmeng Zhou*[a], Hua Wang[a], Douglas Thomson[b], Euan McGookin[b], Xiaohong Guo[c]

[a]*College of Aerospace and Engineering, National University of Defense Technology, Changsha 410073, China*

[b]*School of Engineering, University of Glasgow, Glasgow, G12 8QQ, UK*

[c]*Xiaan Satellite Control Center of China, Xiaan 710000, China*

Abstract

Fault analysis of man-in-loop systems is a valuable issue worthy of being studied, especially in projects including high risk and high investment like manned space missions. Spacecraft sometimes must have the fault tolerance to complete their task even after errors occurring. Inverse simulation was previously proved to achieve manually rendezvous and docking (RVD) successfully. The aim of this paper is to demonstrate the potential applications of inverse simulation to undertake the thruster fault analysis and reconfigurations in manned RVD mission. Firstly, the inverse simulation system is established in a model predicted control structure. Then, the astronauts' operational strategy is analyzed through the thruster fault simulation, and an operational rate factor is proposed to assess the failure risk. In addition, the original configuration is transformed to strengthen the resistance under consideration of the fault tolerance. The comparative results indicate that the modified configuration can improve the performance effectively and then guarantee the success of the mission.

Key words

Manually controlled RVD; MPC structured inverse simulation; Failure mode and effect analysis; Risk Classification; Reconfiguration

* Corresponding author.

Email address: zhouwanmeng13@nudt.edu.cn (W. M. Zhou).

Nomenclature

$\boldsymbol{a_{cha}}$	acceleration vector of chaser	m/s^2
$\boldsymbol{a_{tar}}$	acceleration vector of target	m/s^2
a_f	components of $\boldsymbol{a_{cha}}$ - $\boldsymbol{a_{tar}}$ in Hill coordinate system;	m/s^2
x, y, z	relative positions	m
R_{tar}	distance vector between the target and the earth center	m
μ	gravity constant	
ω_{tar}	angular velocity of the target orbit	rad/s
$\boldsymbol{\Phi(t, t_0)}$	state transforming matrix	
$\boldsymbol{\Phi_u(t, t_0)}$	input transforming matrix	
$\tau=\Delta t$	simulation time step t-t_0	s
$\boldsymbol{C_{bh}}$	transform matrix from body coordinate system to Hill coordinate system	
$\boldsymbol{C_{tb}}$	transform matrix from measurement coordinate system to body coordinate system	
θ_{az}	azimuth	rad
θ_{el}	elevation	rad
ϕ, ψ, θ	roll angle, yaw angle, pitch angle	rad
$\boldsymbol{I}$	rotational inertia matrix	kg.m^2
$\boldsymbol{M}$	external moment vector	N.m
$\boldsymbol{\omega}$	relative angular velocity vector	rad/s
x_t, y_t, z_t	target mass center coordinates in the measurement coordinate system	m
x_s, y_s, z_s	measurement center coordinates in the Hill coordinate system	m
ρ	slope distance of the target mass center	m
$\boldsymbol{p}$	vector from target mass center to chaser mass center	m
$\boldsymbol{p_s}$	sensor installing vector	m
$\boldsymbol{p_t}$	vector from the measurement center to the target mass center	m
$\lvert\theta_{az}\rvert_{\max}$	maximum azimuth angle	°
$\lvert\theta_{el}\rvert_{\max}$	maximum elevation angle	°
$\lvert\psi\rvert_{\max}, \lvert\theta\rvert_{\max}$	maximum attitude error	°
$\lvert y^*\rvert, \lvert z^*\rvert$	maximum offset	m
$\pm\dot{\theta}_s, \pm\dot{\theta}_l.$	border parameters of the switching lines	rad/s
d, δ, a_0	switching line parameters	
btc_1, btc_2, btc_3	opening time parameters	
m	mass of the propellant	kg
u_{max}	maximum thrust	m/s^2
u^*	outputs of the inverse simulation	m/s^2
$\hat{\boldsymbol{x}}(t)$	predicted state in one step	

$\hat{\boldsymbol{u}}$	inputs in one step (t-t_0)	m/s^2
$\Delta\tau$	opening time in one step τ	s
$n\Delta t$	n numbers of inverse simulation step	s
k_t ,k_f	time sensitivity factor and acceleration sensitivity factor	
k	sensitivity factor of the system	
J	minimum cost function	
$\boldsymbol{Q}$	coefficient matrix reflecting the weighs of different components of states	
P_{thrust}	basic thruster amount	
k_p	operational pulse rate	

1 Introduction

The established manually controlled rendezvous and docking (RVD) system considered in this paper is composed of target spacecraft, chaser spacecraft, astronauts, sensor, and thrusters [1]. The orbit control and attitude control are completed by astronauts and controllers respectively. During the rendezvous process, astronauts can adjust positions and velocities of the chaser according to the relative information obtained from various sensors systems in order to achieve the final docking [2].

The modeling and analysis methods of man-in-loop dynamics system can be classified into the analytical method [3-6] and the experimental method [7-12]. Due to the safety concerns of astronauts, the fault experiment cannot be conducted in the real environment. Thus, the combined method of the experimental and analytical method is introduced to study the astronauts' operation under circumstances where there is a fault present.

Inverse Simulation (IS) is a technique to determine the required control inputs needed to achieve specified desired response, the aim of which is to calculate the required inputs of certain maneuvers, for example, the stick operation of the pilots [13]. Inverse simulation in the helicopter design stage is called "desk top flight test" [14], as it can simulate some specific testing flight and obtain the pilot's operations using models and some experimental data. This technique can be regarded as a method that combines experiment with analysis and is different from traditional simulation methods, in that it can acquire more flight information than open-loop or off-line design simulation methods [14, 15]. In the previous research, an IS has been

proved to reproduce the astronaut's operation successfully [16], while this paper aims at investigating the possibility of IS in analyzing the handling qualities in faulty conditions. After considering precision, efficiency, and stability of different algorithms [17-20], the model predictive control (MPC) [21] structured IS technique is chosen for the thruster fault simulation of the manually controlled RVD. Based on the simulation results, the operational strategy and the tolerance border of the system are studied and the thruster configuration is further designed.

Considerable research activities in Spacecraft design has been concerned with the configuration design of thrusters. As early as 1969, Crawford [22] proposed the linear programming method to design the time minimum and fuel minimum configurations. Then, Hwang et al. [23] designed the upper loaded stage using particle swarm optimization to gain the biggest achievement of control commands. Wang et al. [24] proposed an index representing for the limitation of control ability as a design factor for the thruster configuration. Moreover, there are some other investigations about redundant online allocation [25-28] and coupling control with limited thrusters [29].

Configuration design not only includes the installing positions and orientations of thrusters but also the choice of the thruster type and control allocation strategy. The focus of this paper is the improvement of initial designed configuration in order to make RVD system resistant to the thruster faults. Wiktor [30] proposed the concept of minimum control authority and proved that the configuration is sufficient to the control mission when the amplitudes of the disturbing force and moment are in the

limitation of the minimum control authority. However, there are some other cases when the mission is still controllable with the disturbance out of the limitation. In these cases, astronauts sometimes can still complete the mission by some specific compensations even though the disturbing force and moment caused by the fault thruster are beyond the minimum control authority. The manually controlled system has the characters of robustness, discreteness, nonlinearity, and uncertainty. Traditional methods using eigenvalues analysis and stability criterions are too complex for this system to determine the border of controllable disturbance. One effective way to solve this problem is to simulate directly to find the mechanism behind the mission failure. According to the IS results, the modified configuration can be proposed to improve the system resistance to the thruster fault.

This paper describes the application of IS to the analysis of thruster configuration through the following structure:

In the second section, the RVD model and attitude controller are established and then are integrated into RVD IS system; the third section introduces the original configuration and the fault modes of thrusters, and interprets the operation strategy and the physical workloads under both *single-axis* fault and *multi-axis* fault; in the fourth section，the modified configuration is proposed and verified according to fault simulation results; the last section concludes all the research findings of this paper.

2 Modeling of Manually controlled RVD

2.1 RVD dynamics and kinematics modeling

The coordinate systems and parameters used in this paper are shown in Fig. 1.

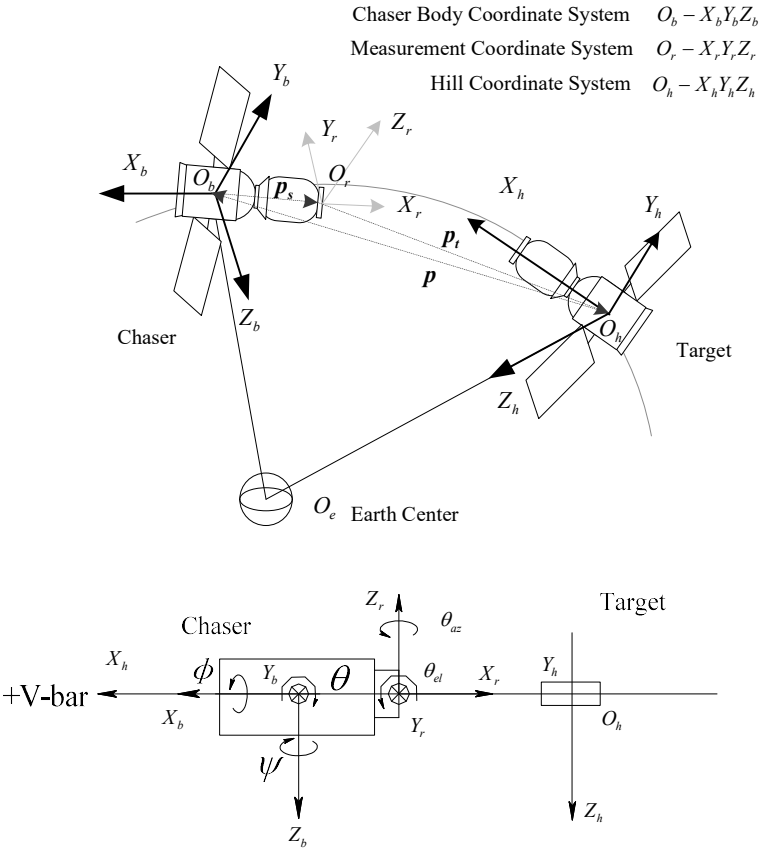

Fig. 1. Coordinate systems and parameters.

$\boldsymbol{p}$ refers to the vector from target mass center to chaser mass center. $\boldsymbol{p_s}$ refers to the installing vector of the sensor. $\boldsymbol{p_t}$ refers to the vector from the measurement center to the target mass center. The Hill coordinate system is defined with z_h-axis orienting to the earth center, x_h-axis orienting to the velocity, and y_h-axis submitted to right hand regulation. All axes of body coordinate system are orienting to the body main axes. z_r-axis of measurement coordinate system is in the same direction of y_r-axis in body coordinate system. The directions of x_r-axis and y_r-axis are opposite to the

directions of x_b-axis and z_b-axis, respectively. ϕ, θ, and ψ refer to the attitude parameters. θ_{az} and θ_{el} are the angles of the view.

Without any assumptions, the relative dynamics equations [2] are given by

$$\begin{cases} \ddot{x} - 2\omega_{tar}\dot{z} - \omega_{tar}^2 x - \dot{\omega}_{tar} z + \dfrac{\mu}{[(R_{tar}-z)^2 + x^2 + y^2]^{3/2}} x = a_{fx} \\ \ddot{y} + \dfrac{\mu}{[(R_{tar}-z)^2 + x^2 + y^2]^{3/2}} \dot{y} = a_{fy} \\ \ddot{z} + 2\omega_{tar}\dot{x} - \omega_{tar}^2 z + \dot{\omega}_{tar} x + \dfrac{\mu}{R_{tar}^2} - \dfrac{\mu}{[(R_{tar}-z)^2 + y^2 + x^2]^{3/2}} (R_{tar} - z) = a_{fz} \end{cases} \tag{1}$$

where a_f refers to the components of $\boldsymbol{a_{cha} - a_{tar}}$ in the Hill coordinate system; x, y, and z refer to the relative positions; R_{tar} refers to the distance vector between the target and the earth center; μ is the gravity constant; ω_{tar} is the angular velocity of the target orbit. Given the assumptions that the earth is spherical and uniform (i.e. without consideration of gravity disturbance), the target travels around the near circle orbit, and the distance between the two spacecraft is far less than the orbit radius. Eq.(1) can then be simplified as

$$\begin{cases} \ddot{x} - 2\omega_{tar}\dot{z} = u_x \\ \ddot{y} + \omega_{tar}^2 y = u_y \\ \ddot{z} + 2\omega_{tar}\dot{x} - 3\omega_{tar}^2 z = u_z \end{cases} \tag{2}$$

where u refers to the component of the control input in the Hill coordinate system. The above equations, according to the state function form, can be transformed into

$$\boldsymbol{x}(t) = \boldsymbol{\Phi}(t, t_0)\boldsymbol{x}(t_0) + \int_{t_0}^{t} \boldsymbol{\Phi_u}(t, \tau)\boldsymbol{u}(\tau)\, d\tau \tag{3}$$

where $\boldsymbol{\Phi(t, t_0)}$ is the state transforming matrix and $\boldsymbol{\Phi_u(t, t_0)}$ is the input transforming matrix, which are shown as

$$\boldsymbol{\Phi}(t,t_0)=\begin{bmatrix} 1 & 6\left(s-\omega_{tar}\tau\right) & 0 & \left(4s-3\omega_{tar}\tau\right)/\omega_{tar} & 2(c-1)/\omega_{tar} & 0 \\ 0 & 4-3c & 0 & 2(1-c)/\omega_{tar} & s/\omega_{tar} & 0 \\ 0 & 0 & c & 0 & 0 & s/\omega_{tar} \\ 0 & 6\omega_{tar}\left(c-1\right) & 0 & 4c-3 & -2s & 0 \\ 0 & 3\omega_{tar}s & 0 & 2s & c & 0 \\ 0 & 0 & -\omega_{tar}s & 0 & 0 & c \end{bmatrix} \tag{4}$$

$$\boldsymbol{\Phi}_{\boldsymbol{u}}(t,t_0)=\begin{bmatrix} \left(4s-3\omega_{tar}\tau\right)/\omega_{tar} & 2(c-1)/\omega_{tar} & 0 \\ 2(1-c)/\omega_{tar} & s/\omega_{tar} & 0 \\ 0 & 0 & s/\omega_{tar} \\ 4c-3 & -2s & 0 \\ 2s & c & 0 \\ 0 & 0 & c \end{bmatrix} \tag{5}$$

where $\tau=\Delta t=t-t_0$, $s=\sin\omega_{tar}\tau$, and $c=\cos\omega_{tar}\tau$.

Assumed that the inputs are constant in τ, Eq.(3) can be modified into

$$\boldsymbol{x}(t)=\boldsymbol{\Phi}\left(t,t_0\right)\boldsymbol{x}\left(t_0\right)+\boldsymbol{\Phi}_{\boldsymbol{u}}\left(t,t_0\right)\boldsymbol{u}\left(t_0\right) \tag{6}$$

where $\boldsymbol{\Phi_u(t, t_0)}$ is

$$\boldsymbol{\Phi}_{\boldsymbol{u}}(t,t_0)=\begin{bmatrix} 4\left(1-c\right)/\omega_{tar}^2 & 2(s-\omega_{tar}\tau)/\omega_{tar}^2 & 0 \\ 2(\omega_{tar}\tau-s)/\omega_{tar}^2 & \left(1-c\right)/\omega_{tar}^2 & 0 \\ 0 & 0 & \left(1-c\right)/\omega_{tar}^2 \\ \left(4s-3\omega_{tar}\tau\right)/\omega_{tar} & 2\left(c-1\right)/\omega_{tar} & 0 \\ 2\left(1-c\right)/\omega_{tar} & s/\omega_{tar} & 0 \\ 0 & 0 & s/\omega_{tar} \end{bmatrix} \tag{7}$$

The expected control input vector $\boldsymbol{u}^*$ can be expressed in the Hill coordinate system as

$$\begin{bmatrix} u_x \\ u_y \\ u_z \end{bmatrix}=\boldsymbol{C}_{\boldsymbol{bh}}(\phi,\theta,\psi)\begin{bmatrix} u_x^* \\ u_y^* \\ u_z^* \end{bmatrix} \tag{8}$$

where $\boldsymbol{C_{bh}}$ refers to the transform matrix from the body coordinate system to the Hill coordinate system. The equation can be further simplified when ignoring the second order small quantities as

$$\begin{bmatrix} u_x \\ u_y \\ u_z \end{bmatrix} = \begin{bmatrix} 1 & -\psi & \theta \\ \psi & 1 & -\phi \\ -\theta & \phi & 1 \end{bmatrix} \begin{bmatrix} u_x^* \\ u_y^* \\ u_z^* \end{bmatrix} \tag{9}$$

The attitude dynamics equations are generally given by

$$\boldsymbol{I} \cdot \dot{\boldsymbol{\omega}} + \boldsymbol{\omega} \times \left(\boldsymbol{I} \cdot \boldsymbol{\omega} \right) = \boldsymbol{M} \tag{10}$$

where $\boldsymbol{I}$ is the rotational inertia matrix, $\boldsymbol{M}$ is the external moment vector, and $\boldsymbol{\omega}$ is the relative angular velocity vector. Each axis of body coordinate system is along the direction of principle axis of inertia. The components of kinematics equations are then given as

$$\begin{bmatrix} \omega_x \\ \omega_y \\ \omega_z \end{bmatrix} = \begin{bmatrix} 1 & 0 & -\sin\theta \\ 0 & \cos\phi & \cos\theta\sin\phi \\ 0 & -\sin\phi & \cos\theta\cos\phi \end{bmatrix} \begin{bmatrix} \dot{\phi} \\ \dot{\theta} \\ \dot{\psi} \end{bmatrix} - C_{hb}(\phi,\theta,\psi) \begin{bmatrix} 0 \\ -\omega_{tar} \\ 0 \end{bmatrix} \tag{11}$$

The coordinates of the target mass center O_h in the measurement coordinate system O_r-$X_rY_rZ_r$ are set to (x_t, y_t, z_t), and then the slope distance of the target mass center ρ, azimuth θ_{az}, and elevation θ_{el} can be calculated from

$$x_{\mathrm{t}} = \rho\cos\theta_{\mathrm{el}}\cos\theta_{\mathrm{az}},\ y_{\mathrm{t}} = \rho\cos\theta_{\mathrm{el}}\sin\theta_{\mathrm{az}},\ z_{\mathrm{t}} = \rho\sin\theta_{\mathrm{el}} \tag{12}$$

The vector from target mass center to the chaser mass center $\boldsymbol{p}$, the installing vector of sensor $\boldsymbol{p_s}$, and the vector from the measurement center to the target mass center $\boldsymbol{p_t}$ connect from end to end, i.e. $\boldsymbol{p} + \boldsymbol{p_t} + \boldsymbol{p_s} = \boldsymbol{0}$, which is shown in Fig.1. The components of the above equation can be given by

$$\begin{bmatrix} x \\ y \\ z \end{bmatrix} = -\boldsymbol{C_{bh}}(\phi,\theta,\psi)\boldsymbol{C_{tb}} \begin{bmatrix} x_t \\ y_t \\ z_t \end{bmatrix} - \boldsymbol{C_{bh}}(\phi,\theta,\psi) \begin{bmatrix} x_s \\ y_s \\ z_s \end{bmatrix} \tag{13}$$

where $\boldsymbol{C_{tb}}$ is the transforming matrix from measurement coordinate system to body coordinate system. Substitute Eq.(12) into Eq.(13) and ignore the two order small

quantity, the relationship between measurement parameters and the relative motion state can then be expressed as

$$\begin{bmatrix} x \\ y \\ z \end{bmatrix} \approx \begin{bmatrix} \rho - x_s \\ \rho \tan\left(\psi - \theta_{\text{az}}\right) - y_s \\ -\rho \tan\left(\theta - \theta_{\text{el}}\right) - z_s \end{bmatrix} \tag{14}$$

Eq.(14) can be used to determine the actual azimuth and elevation angle, which is shown as below

$$\theta_{az} = \psi - \arctan(\frac{y + y_s}{\rho}), \theta_{el} = \theta - \arctan(\frac{z + z_s}{\rho}) \tag{15}$$

Fig. 2 illustrates the relationship of the sensor view and the target in the standard case, attitude error case and the position error case.

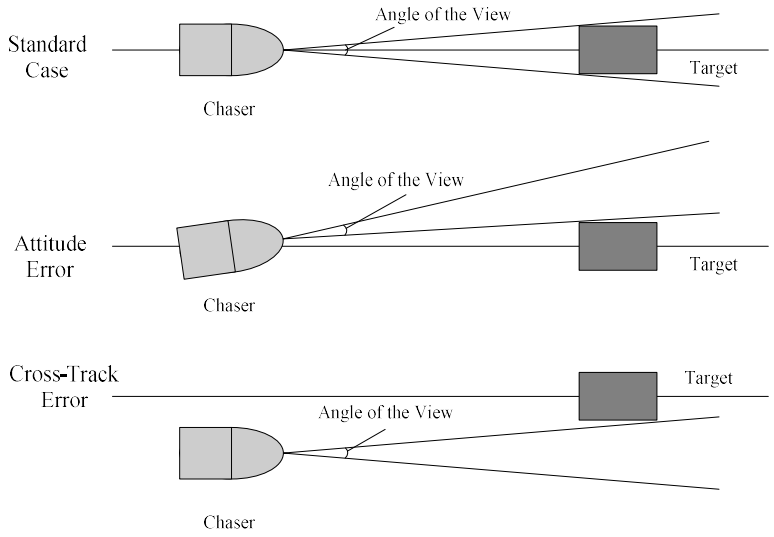

Fig. 2. Target and sensor view relationship diagram.

According to the maximum azimuth $|\theta_{az}|_{\max}$ and elevation $|\theta_{el}|_{\max}$, and the maximum attitude error $|\psi|_{\max}$ and $|\theta|_{\max}$, the maximum offset $|y^*|$ and $|z^*|$ can be expressed as

$$\left|y^*\right| = \rho(\left|\psi\right|_{\max} - \left|\theta_{\text{az}}\right|_{\max}) - y_s, \left|z^*\right| = \rho(\left|\theta\right|_{\max} - \left|\theta_{\text{el}}\right|_{\max}) - z_s \tag{16}$$

where the ranges of the attitude error $|\psi|_{\max}$ and $|\theta|_{\max}$ are pre-designed according to the docking requirements. Eq.(16) can be used to determine maximum lateral offsets

and the RVD corridor is then determined. The target within the corridor stays in the sensor view even if the attitudes reach the maximum values.

The attitudes are controlled by the automatic control scheme, as detailed in Appendix A. Meanwhile astronauts should cooperate with the automatic controller to keep the chaser in the limitation of the largest lateral offset.

2.2 Inverse simulation method in RVD

The IS method used here has a similar structure to MPC. The inverse link, the IS steps, and the forward simulation steps in the IS method are regarded as the predictive model [20]，the receding horizon, and control period in MPC, respectively. The main difference of outcomes between IS and MPC is whether the control outputs in one receding horizon are constant or not. The outputs of the inverse loop are constant, while MPC chooses the first control signal of the optimized sequences in every loop as the control input. Thus, the MPC structured IS technique retains properties of MPC to achieve the online and multi-variable control. At the same time, properly simplified an inverse model with the high-order forward model can obtain precise results and improve the simulation efficiency [20].

The structure of IS includes IS link, forward simulation link, measurement link, and data offered link, shown in Fig. 3.

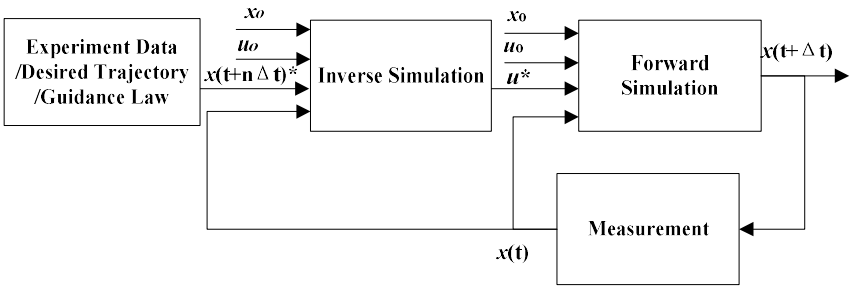

Fig. 3. Inverse simulation structure.

In this IS structure, the internal loop is IS, and the forward simulation and measurement link belong to the external loop. The current state of spacecraft $x(t+\Delta t)$ is produced by the external loop and transmitted to the internal loop through the measurement link. The expected state $x(t+n\Delta t)^*$ is produced from the experimental data or the designed guidance law. The term $n\Delta t$ refers to the n numbers of IS step Δt. The desired control input u^* can be calculated according to the current forward simulation results $x(t+\Delta t)$ and the desired states $x(t+n\Delta t)^*$. The continuous control signal is then discretized using the pulse width pulse frequency theory, as detailed in Appendix B. Then, the discrete control input is passed into the forward simulation link to start the next simulation loop.

According to the numbers of dimensions of inputs and outputs, the control inputs calculation can be classified into normal, sufficient and insufficient problems depending on that the dimension of the input is equal, bigger or smaller than that of the output. To establish a general IS structure, a uniform formulation of these three kinds of problems is required. The state function in one step can be given by

$$\hat{\boldsymbol{x}}(t) = \boldsymbol{\Phi}\left(t, t_0\right)\boldsymbol{x}\left(t_0\right) + \int_{t_0}^{t} \boldsymbol{\Phi}_{\boldsymbol{u}}\left(t, \tau\right)\hat{\boldsymbol{u}}\left(\tau\right)d\tau \tag{17}$$

where $\hat{\boldsymbol{x}}(t)$ refers to the predicted value in one step. If the inputs $\hat{\boldsymbol{u}}$ keep constant in one step (t-t_0), the equation above can be expressed as

$$\hat{\boldsymbol{x}}(t) = \boldsymbol{\Phi}\left(t, t_0\right)\boldsymbol{x}\left(t_0\right) + \boldsymbol{\Phi}_{\boldsymbol{u}}\left(t, t_0\right)\hat{\boldsymbol{u}}\left(t_0\right) \tag{18}$$

For the normal equations, $\boldsymbol{u}(k)$ can be calculated directly, while the sufficient and insufficient equations should be calculated as the follow steps. The IS is to find the most suitable input $\hat{\boldsymbol{u}}$ to get the minimum cost function J between expected and predicted states, i.e.

$$J = (\boldsymbol{x}_c - \boldsymbol{x})^T (\boldsymbol{Q}^{\frac{1}{2}})^T \boldsymbol{Q}^{\frac{1}{2}} (\boldsymbol{x}_c - \boldsymbol{x}) \tag{19}$$

where $\boldsymbol{x}$ refers to the predicted state of the input $\hat{\boldsymbol{u}}$ within one receding horizon, $\boldsymbol{x}_c$ refers to the expected state, $\boldsymbol{Q}$ refers to the coefficient matrix reflecting the weighs of different components of states. Eq.(19) is discretized to

$$J(\boldsymbol{u}(k)) = (\boldsymbol{x}_c(n+k) - \boldsymbol{x}(n+k))^T \boldsymbol{Q} (\boldsymbol{x}_c(n+k) - \boldsymbol{x}(n+k)) \tag{20}$$

The solution of the sufficient and insufficient equations can both be calculated to get the minimum of $J(\boldsymbol{u}(k))$. According to the pseudo-inverse theory, the weighed minimal norm least square solution is given by

$$\boldsymbol{u}(k)_{LS} = (\boldsymbol{\Phi}_u(n\tau)^T \boldsymbol{Q} \boldsymbol{\Phi}_u(n\tau))^{-1} \boldsymbol{\Phi}_u(n\tau)^T (\boldsymbol{x}_c(n+k) - \boldsymbol{\Phi}(n\tau)\boldsymbol{x}(k)) \tag{21}$$

Verification is conducted by the independently developed 9 degrees of freedom manually controlled RVD experiment platform in National University of Defense Technology [31]. The platform utilizes the console to record all the operations and motion states data during the process. The experimental data can be used as the input of the IS, and the results are compared with recorded operational data to verify the established IS model [32].

2.3 Application of IS structure in RVD

Same as the aircraft, during the approaching phase of RVD, the spacecraft sometimes need to be manually controlled to achieve some specific translational motion (or the rotational motion at the same time). In the manually controlled RVD system, astronauts are replaced by the inverse model. Given out the desired mission trajectories of RVD, the simulation result is then calculated using inverse simulation technology, shown as Fig. 3. The applications of IS on RVD system fall into two aspects. One application is the initial handling qualities assessment (details can be

seen in [33]). The other application is the failure effect analysis and allocation design. Few research concerned about the manually controlled strategy under the failure circumstance and the further allocation design. The process of the allocation design can be illustrated in Fig. 4.

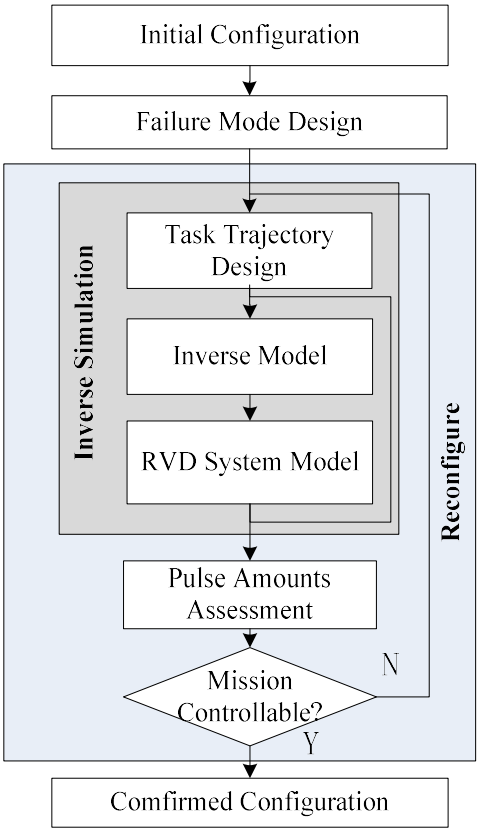

Fig. 4. Guideline for the thruster configuration design.

When some of the actuators broke down, the inverse model was utilized to control the spacecraft to move along the desired trajectory. According to the pulse amounts, operation strategies for astronauts to complete the mission can be concluded. The allocation of the thruster can then be further reconfigured against different failure scenarios.

3 Failure mode and effects analysis

3.1 Original configuration and failure modes

The thruster used in the mission is an electromagnetic-type actuator. The coil current lifts the flow valve to jet the propellant [34, 35]. Failures in any link could cause a thrust error. The covering strategy is to shut down the detected faulty thrusters. Thus, the thrust fault is equally abrupt and permanent. All the faults mentioned later mean the thrusts descent to zero. The original arrangement is shown in Fig. 5, which is composed of one orbit maneuver engine; six bidirectional attitude control thrusters: a, a˜, b, b˜, c, c˜; and twelve unidirectional translational control thrusters: d1, d1˜, d2, d2˜, e1, e1˜, e2, e2˜, f1, f1˜, f2, f2˜.

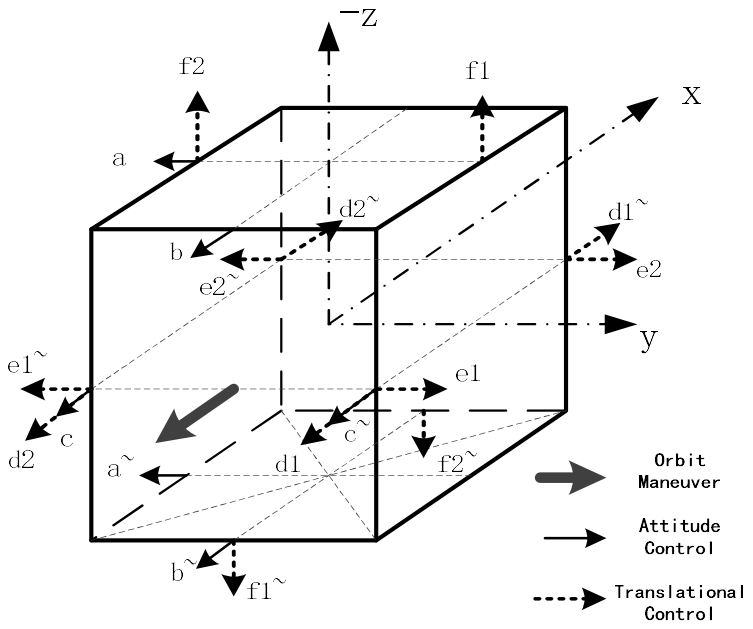

Fig. 5. Original thruster configuration.

The switching signal is designed according to the configuration. The logical relationships between switching signals and control signals are shown in Table 1.

Table 1

Comparison table of control signals and switching signals.

Thruster Symbols		*x*-axis Control			*y*-axis Control			*z*-axis Control		
		0	1	-1	0	1	-1	0	1	-1
Attitude Thruster	a	0	1	-1	-	-	-	-	-	-
	a~	0	-1	1	-	-	-	-	-	--
	b	-	-	-	0	-1	1	-	-	-
	b~	-	-	-	0	1	-1	-	-	-
	c	-	-	-	-	-	-	0	1	-1
	c~	-	-	-	-	-	-	0	-1	1
x-axis Orbit Thruster	d1	0	1	0	-	-	-	-	-	-
	d2	0	1	0	-	-	-	-	-	-
	d1~	0	0	1	-	-	-	-	-	-
	d2~	0	0	1	-	-	-	-	-	-
y-axis Orbit Thruster	e1	-	-	-	0	0	1	-	-	-
	e2	-	-	-	0	0	1	-	-	-
	e1~	-	-	-	0	1	0	-	-	-
	e2~	-	-	-	0	1	0	-	-	-
z-axis Orbit Thruster	f1	-	-	-	-	-	-	0	1	0
	f2	-	-	-	-	-	-	0	1	0
	f1~	-	-	-	-	-	-	0	0	1
	f2~	-	-	-	-	-	-	0	0	1

There are two operational states for unidirectional thruster in the table, i.e. 0 refers to thruster closing and 1 refers to thruster opening. The attitude control thrusters have three operational states i.e. -1 refers to the negative direction opening, 1 refers to the positive direction opening, and 0 refers to thruster closing. The opening signal of each thruster is determined once the configuration and the control signal are defined.

This paper considers the faults in the orbit control thrusters as it relates to the astronaut's operation directly. When all the thrusters in any axis are broken down, the chaser must run in the passive or active modes to avoid flying into the forbidden zone [36-38]. The other faulty cases when the astronauts can still achieve the docking with

the remaining thrusters are mainly discussed here. The error modes can be separated into *single-axis* error, *multi-axis* error based on the axis or into *one thruster error*, *two thrusters error* and so on based on the numbers of faulty thrusters. Table 2 gives out the error modes of orbit control thrusters in three axes, × refers to the error and ○ refers to the normal work.

Table 2
Error modes of orbit control thrusters in three axes.

x-axis Orbit Control Thrusters	d1	×	○	○	○	×	×	○	○
	d2	○	×	○	○	○	○	×	×
	d1~	○	○	×	○	×	○	○	×
	d2~	○	○	○	×	○	×	×	○
y-axis Orbit Control Thrusters	e1	×	○	○	○	×	×	○	○
	e2	○	×	○	○	○	○	×	×
	e1~	○	○	×	○	×	○	○	×
	e2~	○	○	○	×	○	×	×	○
z-axis Orbit Control Thrusters	f1	×	○	○	○	×	×	○	○
	f2	○	×	○	○	○	○	×	×
	f1~	○	○	×	○	×	○	○	×
	f2~	○	○	○	×	○	×	×	○

The operational amount is given to represent for the control compensatory degree of astronauts to complete the mission which is an index to indicate the complexity, energy consumption, and risk degree of the mission [10]. The more fuels are consumed, the more operations should be executed. The operational amount is defined as the ratio of control pulse amounts to basic pulse amounts, which is expressed as

$$k_p = \frac{P}{P_{thrust}} \tag{22}$$

where P_{thrust} is the basic thruster amount, P refers to the actual pulse amounts.

3.2 Single-axis fault analysis

IS is utilized to simulate the handling controlled RVD along the designed trajectories for inspecting the operational strategy in different error modes. The simulation setting configuration and initial conditions are listed in Table 3.

Table 3
Simulation settings under fault conditions.

Parameters	Values
Initial Relative Positions	$x = 100.038m, y = -0.0167m, z = -0.023m$
Initial Relative Velocities	$vx = -0.0076\,m/s, vy = 0.131\,m/s, vz = -0.0087\,m/s$
Envelope Size	$2.42m \times 2.42m \times 4m$
Orbit Control Thrust	$60N$
Attitude Control Thrust	$25N$
Basic Pulse Amount	3000
Limitation of θ_{el} and θ_{az}	$-10^{\circ} \sim 10^{\circ}$
Limitation of Attitude Angle	$-1^{\circ} \sim 1^{\circ}$
Sensitive Factor	0.35
Receding Horizon	3
Step	1
Simulation Time	1300s

Fig. 6 shows the trajectories, attitudes and pulses under the nominal conditions. The pulse amounts in three axes are 164, 557, and 856, in which the forward pulse amounts are 114, 230, and 327 respectively.

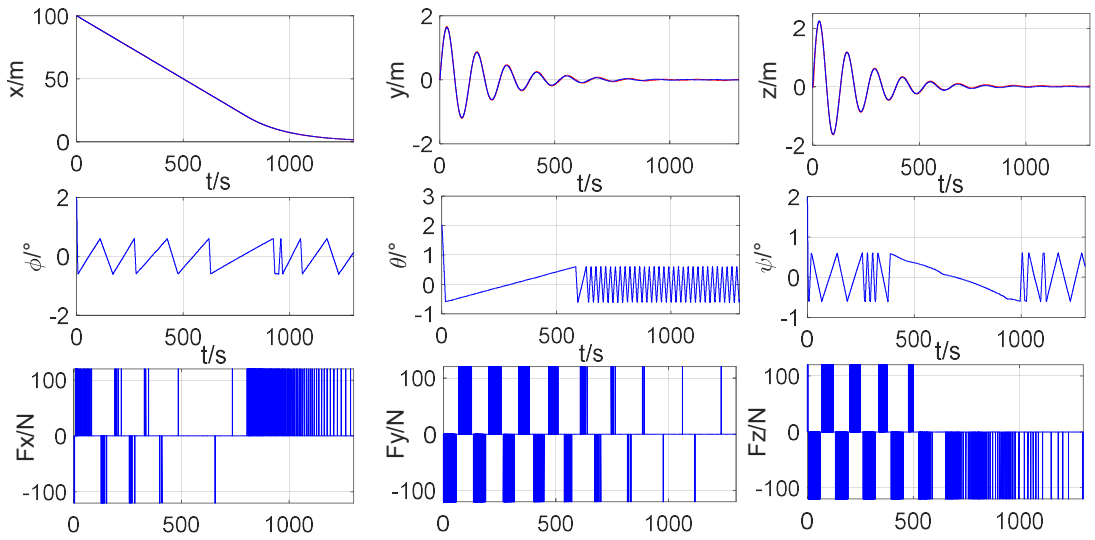

Fig. 6. Simulation results of nominal conditions.

The motion in the *y*-axis is decoupled with the other axes. Comparing with the other axes, the decoupled motion is only affected by the thruster of the y-axis and the regulation of the fault effect is more obvious. Thus, the operational strategy of fault thrusters in the *y*-axis is mainly analyzed here. All the other cases will be listed at the end of this part. Fig. 7 shows the attitude and measurement angles in the *y*-axis. The single thruster fault occurs in thruster e1~， while the double thrusters faults occur in thruster e1 and thruster e1~.

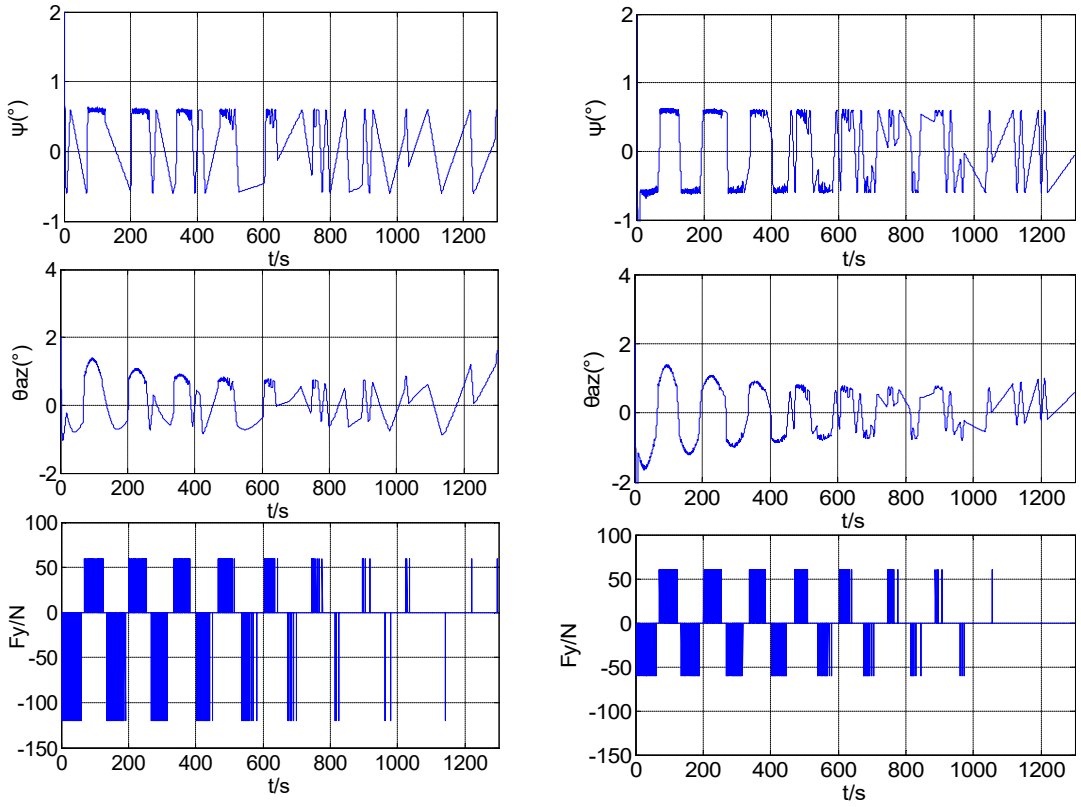

Fig. 7. Simulation results in the case of y-axis thruster faults. (a) faults in thruster e1˜ (b)faults in thruster e1 and e1˜.

The failure of e1˜ can cause the disturbing positive moment in the *z*-axis and the reduction of the forward thrust in the *y*-axis. With the original configuration in Fig 5, the yaw will be increased by the positive disturbing moment and revised by the attitude controller. When *t*=800s, the motion in *x*-axis enters the index damping phase as shown in Fig. 7, and then the *x*-axis thrusters keep opening forward. Table 4 indicates that the astronauts should increase the impulse compensation to overcome the effects of thruster failures.

When thrusters e1 and e1˜ break down, *z*-axis positive moment and decreasing forward thrust are caused by the forward thrust signal in the *y*-axis and vice versa. The opposite effects of positive and negative control signals can produce more symmetrical results, which can be seen in results of yaw and azimuth. Thus, when the

single thruster breaks down, one can consider shutting down a thruster in the opposite direction to produce the symmetrical effects. However, the compensatory effect of double thruster failures in the *y*-axis is more than that of single thruster failure, i.e. the physical workloads of the operator will definitely be increased.

Fig. 8 shows the attitude and measurement angles in the *y*-axis. Fig. 8 (a) shows the results of shutting down in thrusters e2 and e1˜, and Fig. 8 (b) shows the results of shutting down in thrusters e1 and e2˜. The thrust magnitude of both directions in the *y*-axis reduces from 120 N to 60 N.

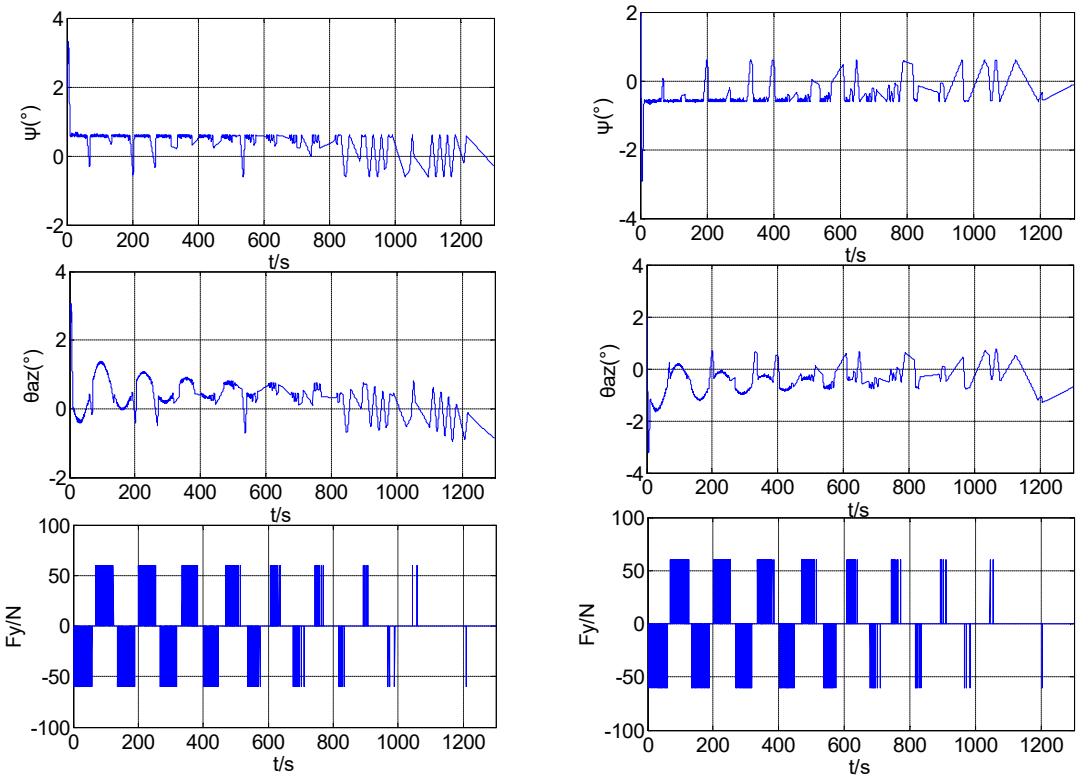

Fig. 8. Simulation results in the case of different side faults of y-axis thrusters. (a) faults in thruster e2 and e1˜ (b) faults in thruster e1 and e2˜.

Fig. 8 indicates that when the different side of the thrusters in one axis break down, the opposite control signals can cause the disturbing moment in the same direction. Compared with the same side fault, the different side fault can lead to larger deviation of the attitude angle. When the spacecraft enters the index damping phase,

the coupling effects from *x*-axis will affect *y*-axis more severely. Figure. 8 (a) shows that the failures of e2 and e1~ can cause the coupling effects on the positive offset in the *y*-axis and azimuth decrease, while Figure. 8 (b) shows the failures of e1 and e2~ can cause the coupling effects on negative offset in *y*-axis and azimuth increase. The physical workloads of the same side and different side failures are equivalent.

According to Eq. (22), the physical workloads and the operational amount of different error modes are calculated and listed in Table 4.

Table 4
Operational amount of the *single-axis* thruster fault.

Fault Thruster	*x*-axis		*y*-axis		*z*-axis		Operational Amount
	+	-	+	-	+	-	
——	114	50	230	327	289	567	0.53
e1~	114	50	464	328	292	568	0.61
e2~	114	50	459	326	289	565	0.60
e1/e1~	116	52	459	645	289	567	0.71
e2/e1~	115	51	458	647	290	568	0.71
e1/e2~	116	52	457	645	289	568	0.71
f1	116	51	231	327	576	567	0.62
f2~	114	50	231	328	288	1131	0.71
f1/f1~	116	51	230	326	579	1088	0.80
f2/f1~	116	51	229	328	577	1088	0.81
f1/f2~	116	51	227	325	577	1089	0.80
f2/f2~	117	52	230	326	576	1088	0.80
d1	230	49	228	325	290	567	0.56
d1~	123	104	231	326	288	564	0.55
d1/d1~	250	105	232	328	288	564	0.59
d2/d1~	251	106	228	323	288	563	0.59
d1/d2~	252	105	229	325	290	569	0.59

The table indicates that the operational impulse amounts are nearly double the amounts of the basic impulse. In the nominal situation, the most pulses are in the *z*-axis, thus the astronauts require most compensatory operations when thrusters in the

z-axis fail down. According to the definition of *risk* in Ref.35, the *risk* is herewith determined by the compensatory amount of the thruster failure, in other words, the larger physical workloads refer to the more severe faults. Thus, the degree of risks can be ranked from the minimum to maximum as: single *x*-axis fault, double *x*-axis faults, single *y*-axis fault, single *z*-axis fault, and double y-axis faults. Double *z*-axis faults are the most severe errors. Eq.(2) can also indicate that *y*-axis motions in the Hill coordinate system are decoupled with the other two axes, but the *z*-axis motions are effected by the gravity and motions in the *x*-axis. Thus, faults in *z*-axis thrusters are much more serious.

3.3 Multi-axis fault analysis

When there are errors in more than one axis, due to the limited attitude control abilities, the astronauts cannot promise the successful completion. In the original configuration, the *x*-axis and *y*-axis failures can both produce a disturbing *z*-axis moment, while the failure in *z*-axis can produce disturbing *x*-axis and *y*-axis moments. Thus, the coupling of *multi-axis* fault mainly refers to the failures of thrusters in *x*-axis and *y*-axis.

Four *multi-axis* fault cases chosen from all the controllable fault circumstances are studied here. The shutting down thrusters are d1, d1~, e1, and e1~; d1, d2~, e1, and e2~; d2, d1~, e2, and e2~; d2, d2~, e2, and e1~. The simulation results of the four cases are shown below.

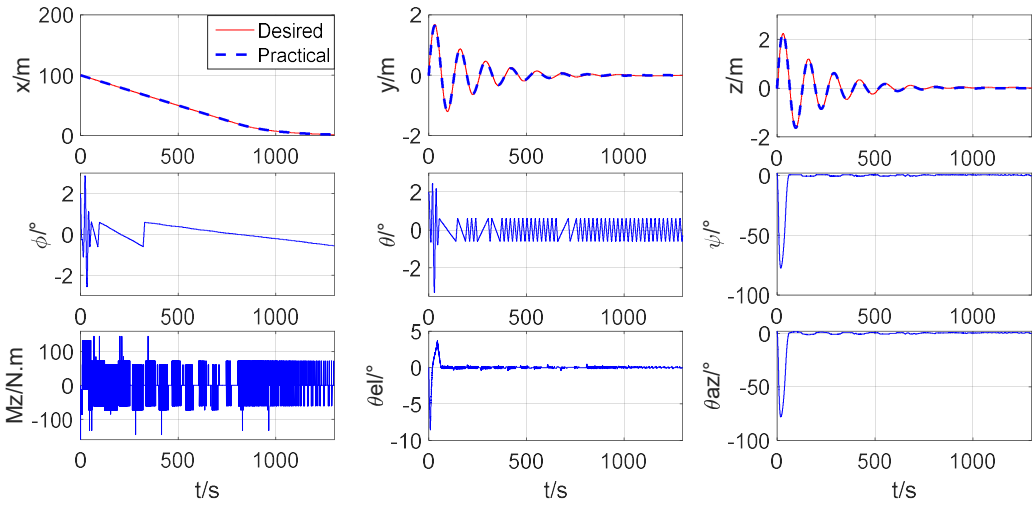

Fig. 9. Simulation results of case 1.

Fig. 9 shows the case with failures of thrusters d1, d1~, e1, and e1~. The azimuth appears to be diverging largely at the beginning, though the controller can eventually control the chaser to follow the expected trajectory. The deviation of the target would lead to the measurement failure if no other sensors were present. The main reason is at the start of the mission negative thrusters in y and x axes are required to open simultaneously. They produce the disturbing moments in the same direction during the period which cause the deviation of the azimuth.

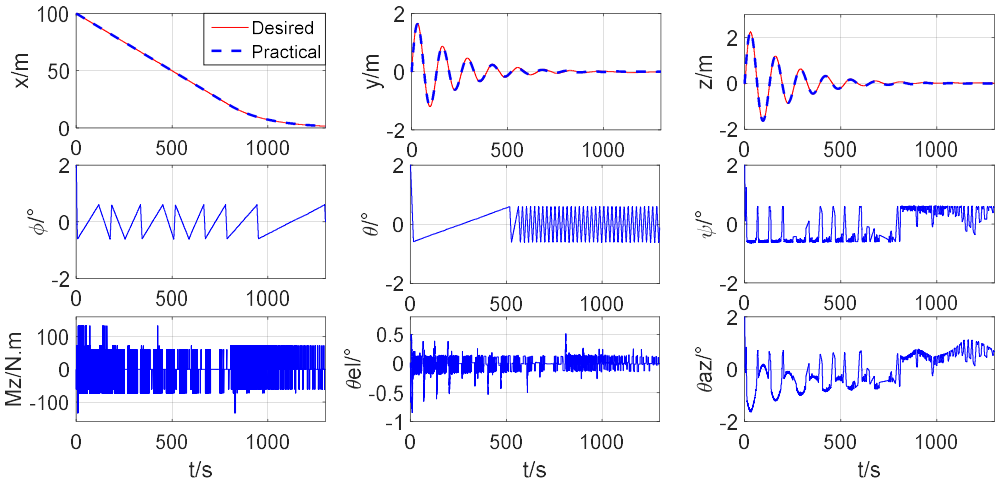

Fig. 10. Simulation results of case 2.

The results of case 2 with the failures of thruster d1, d2~, e1, and e2~ are better than those in case 1. Faults in two axes will produce opposite disturbing moments,

thus the moments produced simultaneously can counteract each other. After 800 seconds, the motion in the *x*-axis enters into the index damping phase and the thrusters keep opening negatively, which produces the positive disturbing moment to increase the azimuth and keep it positive.

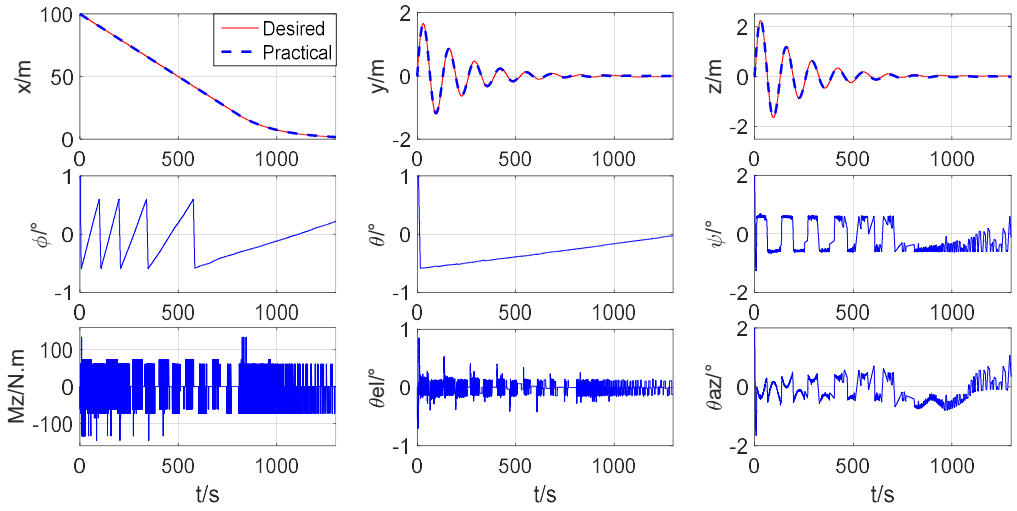

Fig. 11. Simulation results of case 3.

Case 3 is the situation with the failures of thrusters d2, d1~, e2, and e2~, which is opposite of case 2. At first, the negative acceleration in *y*-axis can cause a positive disturbing moment opposite to the disturbing moment caused by *x*-axis thrusters. Thus, the azimuth would not exceed its limitations. After 800s, the continuously negative disturbing moment decreases the azimuth and keeps it below zero.

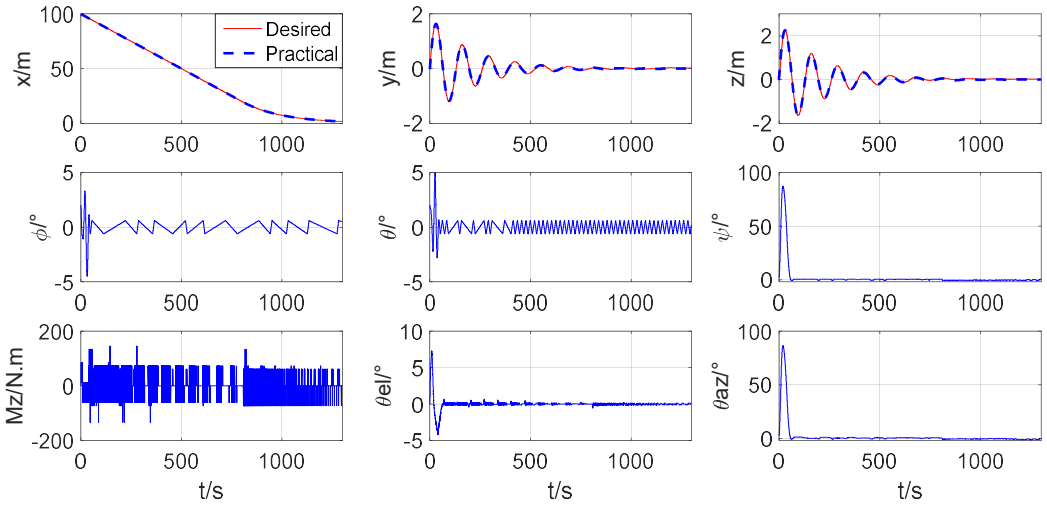

Fig. 12. Simulation results of case 4.

Case 4 is the situation with the failures of thrusters d2, d2~, e2, and e1~. In the beginning, the negative acceleration in the *y*-axis can cause a positive disturbing moment in accordance with the disturbing moment from failures in the *x*-axis. As in case 1, the azimuth exceeds the limitation of the field of view. The mission would fail without other sensors to measure the relative states.

The physical workloads of all the multi-axis faults are listed in Table 5 including four uncontrollable cases.

Table 5

Physical workloads of the *multi-axis* thruster faults.

Faulty Thrusters		*x*-axis		*y*-axis		*z*-axis		Operational Rates
x-axis	*y*-axis	+	-	+	-	+	-	
——	——	114	50	230	327	289	567	0.53
d1/d1~	e1/e1~	245	104	459	620	288	565	0.76
d1/d1~	e1/e2~	245	104	457	622	285	565	0.76
d1/d1~	e2/e1~	251	105	456	641	291	568	0.77
d1/d1~	e2/e2~	252	106	456	641	291	568	0.77
d1/d2~	e1/e1~	250	104	457	643	292	569	0.77
d1/d2~	e1/e2~	250	104	456	643	289	566	0.77
d1/d2~	e2/e1~	——	——	——	——	——	——	——
d1/d2~	e2/e2~	——	——	——	——	——	——	——
d2/d1~	e2/e1~	250	104	457	643	289	567	0.77

d2/d1~	e2/e2~	250	104	458	643	289	567	0.77
d2/d1~	e1/e1~	——	——	——	——	——	——	——
d2/d1~	e1/e2~	——	——	——	——	——	——	——
d2/d2~	e1/e1~	250	104	455	640	290	567	0.77
d2/d2~	e1/e2~	250	104	460	645	289	566	0.76
d2/d2~	e2/e1~	251	104	457	611	293	575	0.76
d2/d2~	e2/e2~	254	107	456	611	292	574	0.76

Table 5 indicates that the compensatory operations of *multi-axis* faults in each axis are equal to those in cases with the *single-axis* fault. The operational rate shows the physical workloads of controllable multiaxial faults are equivalent to those of faults in the *z*-axis. They have the same level of risk. When three or more thrusters break down in *x* and *y* axes, astronauts may not be able to achieve the mission smoothly and the RVD IS system becomes underactuated.

4 Reconfiguration based on risk classification

4.1 Risk classification analysis

The risk could be basically divided into the controllable and uncontrollable risks. The controllable cases are further divided into small deviation and large deviation. The previous results of fault simulations in *single-axis* and *multi-axis* show that the case with the *single-axis* fault is controllable, while the case with multiaxial faults may be uncontrollable. If the effects caused by thruster faults can be considered during the design stage, the configuration can then be improved to mitigate against failures. Risk classification of different *multi-axis* thruster faults is listed in Table 6.

Table 6
Risk classification of different *multi-axis* thruster faults.

Faulty Thrusters	e1/e1~ ***Mz-/Mz+***	e1/e2~ ***Mz-/Mz-***	e2/e1~ ***Mz+/Mz+***	e2/e2~ ***Mz+/Mz-***
d1/d1~ ***Mz+/Mz-***	II	II	I	I
d1/d2~ ***Mz+/Mz+***	I	I	III	III
d2/d1~ ***Mz-/Mz-***	III	III	I	I
d2/d2~ ***Mz-/Mz+***	I	I	II	II

The results of mission-oriented fault simulation show that the negative thrusters should be employed in both *x* and *y* axes at the beginning. Class I refers to the acceptable fault. Class II indicates that the same disturbing moments can cause a large deviation of the yaw and the azimuth. Class III indicates that the directions of disturbing moments caused by thruster faults in both directions in the *x*-axis are same as those of moments caused by *y*-axis thruster failure, the deviation can be even larger which directly leads to the uncontrollable results.

4.2 Further reconfiguration design

The risk degree shows that altitude control thrusters could not resist three or more disturbing moments in one direction Thus, the thruster configuration can be improved in two aspects. On one hand, to enhance the attitude controllability in the *z*-axis to resist the disturbance from the other axes, on the other hand, to reconfigure the thrusters to avoid the superposition of the moments.

To verify the two schemes, the case with shutting down of thrusters d1, d2~, e2, and e1~ is chosen as the comparative simulation case. The fault simulation results of the original configuration are shown in Fig. 13.

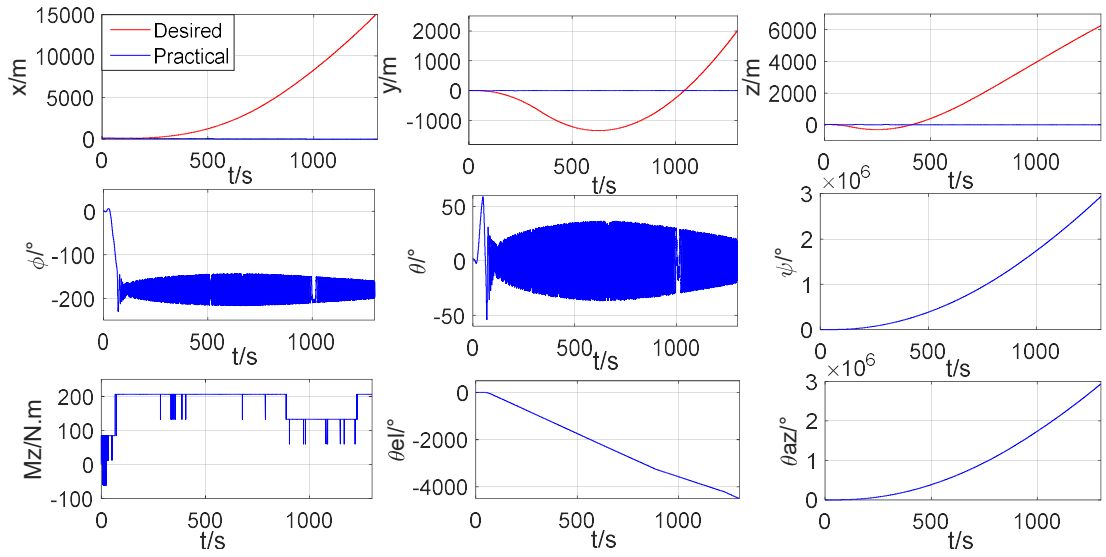

Fig. 13. Fault simulation results of the original configuration.

Scheme I is to improve the control ability of attitude control thrusters from 25 N to 50 N. The results show the large deviation is narrowed into the limitations of the field of view. The whole process becomes controllable.

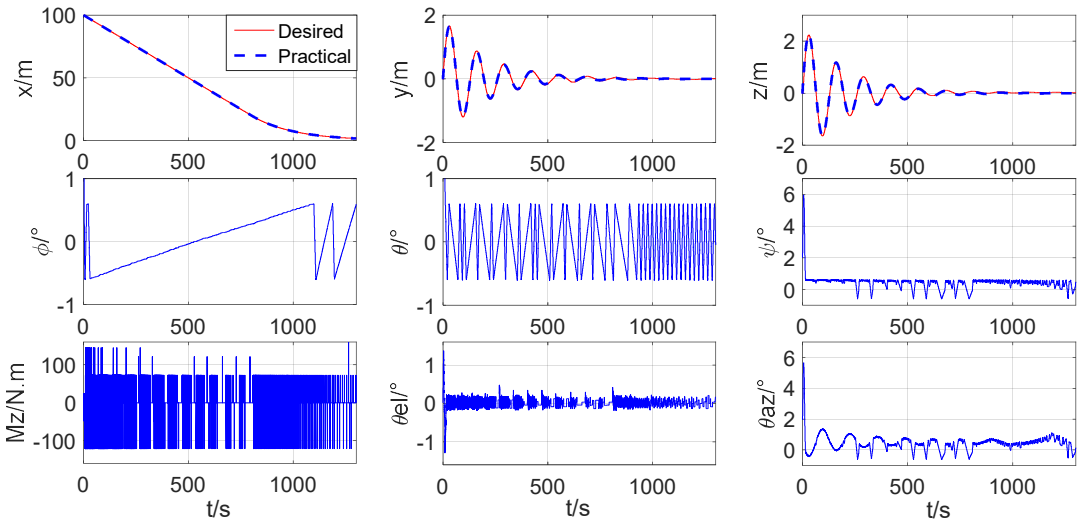

Fig. 14. Fault Simulation of Scheme I.

Scheme II is to reconfigure the orbital control thrusters in the *x*-axis and *y*-axis.to produce the disturbing moments in different axes.

Forward thrusters d1, d2 in the *x*-axis are reinstalled on the vertical *x*-*o*-*z* plane. Backward thrusters e1, e2 in the *y*-axis are reinstalled on the vertical *y*-*o*-*z* plane. The modified configuration is shown in Fig. 15.

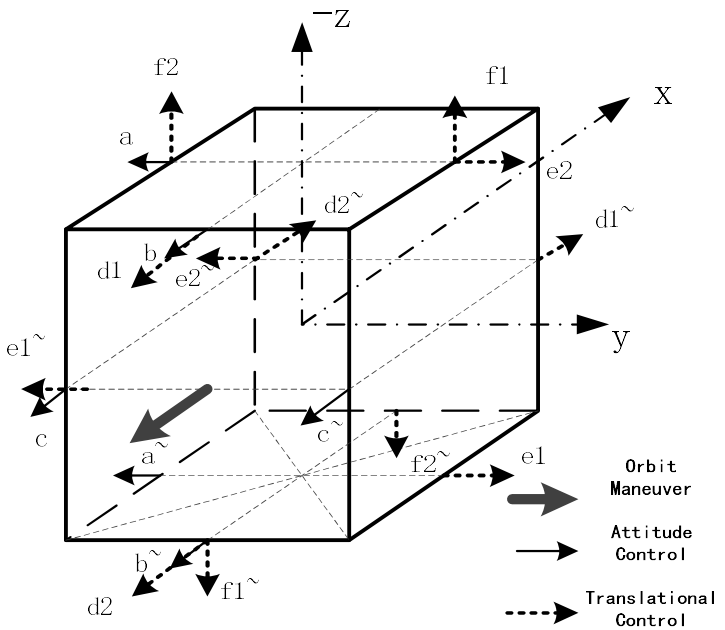

Fig. 15. Modified Configuration of Thrusters.

After the reconfiguration, faults of positive thrusters in the *x*-axis can produce the *y*-axis disturbing moments, and faults of negative thrusters in the *y*-axis can produce

the *z*-axis disturbing moments. The *x*-axis and *y*-axis attitude control moments are larger than that of the *z*-axis. Thus, to adjust the thrusters undertaking most operational pulses in the positive *x*-axis and negative *y*-axis to produce the *y*-axis and *x*-axis disturbing moments respectively can decrease the disturbance in the *z*-axis. The simulation results of the comparative case are shown in Fig. 16.

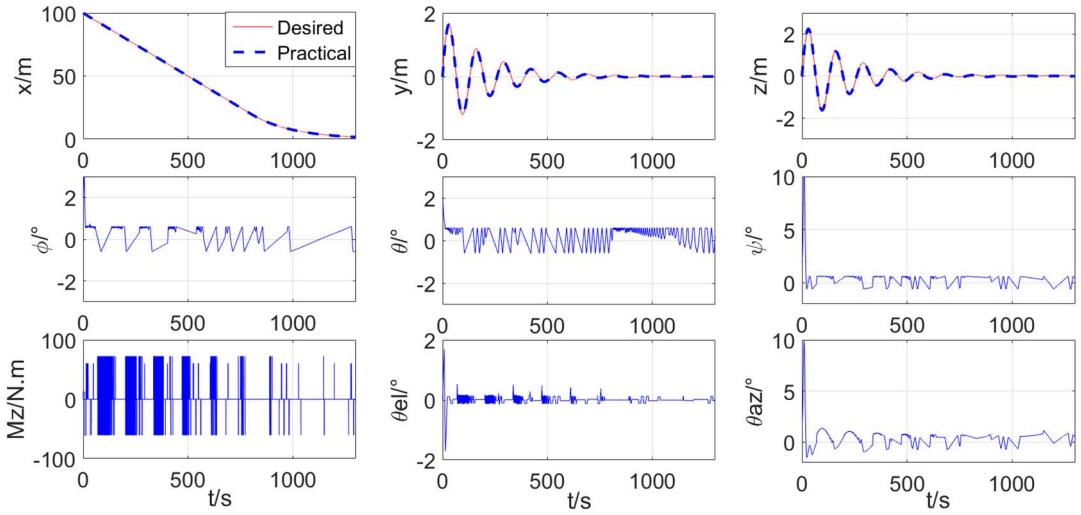

Fig. 16. Fault Simulation of Scheme II.

Both schemes can guarantee the uncontrollable cases with original configuration against failure and become more robust. The maximum tolerant number of faulty thrusters reaches six which means the possibility of mission success under the thruster faults is improved. Comparing the results of the two schemes under the same fault conditions, the opening time of *z*-axis attitude control thrusters in Scheme II is found obviously less than that in Scheme I. It means the physical workload of Scheme II is less, and the scheme is much easier for the astronaut to grasp. Though the azimuth and yaw results of Scheme II within the limitation are little bigger than those with Scheme I, Scheme II cost much fewer fuels to complete the mission. This reflects the trad-off between fuels cost and the precisions. More fuels indicate the less room for effective load and astronauts may feel pressure in the faulty condition, so it is worthy to abandon some precisions to ease the operation and save the fuels under the faulty conditions. In conclusion, Scheme II is superior to Scheme I.

5 Conclusions

Few configuration designs considering the control effect under faulty conditions compare with those focused on the maximum achievement. However, the risk resistance ability is a critical factor for the high risk and high investment projects like manned space missions. Thus, given the unique advantages of inverse simulation in man-in-loop fault simulation，a manually controlled rendezvous and docking inverse simulation system was established to explore a new way to improve the control effect of original configuration under the faulty conditions.

The operational amount was firstly defined to reflect the operation of the astronauts, and based on which the operational strategy and risk grades under *single-axis* and *multi-axis* fault situations through inverse simulation were studied. The rank of risk degree was given out and the physical workloads of controllable multiaxial faults were equivalent to those of the most severe *single-axis* fault cases with double *z*-axis faults. The uncontrollable case was actually caused by the disturbing moments from fault thrusters in the other axes, so the configuration should be well-distributed to avoid disturbances in the same axis or the control thrust of the most influenced axis should be improved. Based on the conclusion, two modified schemes were provided and verified. Both schemes can guarantee the uncontrollable cases against failure and maximize a tolerant number of faulty thrusters, trading off fuels cost and the precisions Scheme II is superior.

The successful implementation of fault analysis and reconfiguration indicates that inverse simulation can be utilized as a general tool for fault analysis and

reconfiguration of the manually controlled systems.

Acknowledgment

We are grateful to Dr. Douglas Thomson for discussions and Dr. Euan McGookin for the language inspection. In addition, we would like to thank the anonymous reviewers for their invaluable feedback. This study was co-supported by the 973 Program (No. 2013CB733100) and the National Natural Science Foundation of China (No. 11272346 and No.11472301).

Conflict of interest statement

The authors declare that no conflict of interest exists.

References

[1] J.Y. Zhou, J.P. Zhou, Z.C. Jiang, Design and validation of novel teleoperation rendezvous and docking system, J. Aerosp. Eng. 27 (5) (2014) 04014017-1–04014017-8.

[2] Y.Z. Luo, J. Zhang, G.J. Tang, Survey of orbital dynamics and control of space rendezvous, Chinese. J. Aeronaut. 27 (1) (2014) 1-11.

[3] D.G. Mitchell, D.B. Doman, D.L. Key, et al., Evolution revolution and challenges of handling qualities, J. Guid. Control. Dyn. 27 (1) (2004) 12-28.

[4] T.P. Neal, R.E. Smith, An in-flight investigation to develop control system design criteria for fighter airplanes, AFFDL-TR-70-74, 1970.

[5] D.T. McRuer, E.S. Krendel, Mathematical models of human pilot behavior, AGARD-AG-188, 1974.

[6] R. Bradley, G. Turner, G. Brindley, Simulation of pilot control activity for the prediction of workload ratings in helicopter/ship operations, 26th European Rotorcraft Forum, The Hague, Netherlands, 2000.

[7] G.E. Cooper, R.P. Harper, Use of pilot rating in the evaluation of aircraft handling qualities, NASA TN D-5153, 1969.

[8] S.G. Hart, L.E. Staveland, Development of NASA-TLX (task load index): results of empirical and theoretical research, human mental workload. P.A. Hancock and N. Meshkati (Eds.), North Holland Press, Amsterdam, The Netherlands, 1988.

[9] D.C. Cheatham, C.T. Hackler, Handling qualities for pilot control of apollo lunar-landing spacecraft, J. Spacecraft and Rockets. 1966, 3 (5): 632-638.

[10] K.D. Bilimoria, E.R. Mueller, C.R. Frost, Handling qualities evaluation of piloting tools for spacecraft docking in earth orbit, J. Spacecraft. Rockets. 48 (5) (2011) 846-855.

[11] R.E. Bailey, E.B. Jackson, J. Arthur, Handling qualities implication for crewed spacecraft operations. IEEE Aerospace Conference Proceedings, 2012.

[12] J.P. Stephens, K.D. Bilimoria, E.R. Mueller, et al., Orion handling qualities during international space station proximity operations and docking, J. Spacecraft. Rockets. 50 (2) (2013) 449-455.

[13] D.G. Thomson, R. Bradley, The principles and practical application of helicopter inverse simulation. Simul. Model. Pract. Th. 6 (1998) 47-70.

[14] D.G. Thomson, R. Bradley, Inverse simulation as a tool for flight dynamics research—principles and applications, Prog. Aerosp. Sci. 42 (3) (2006) 174-210.

[15] D.G. Thomson, C.D. Taylor, N. Talbot, et al., An investigation of piloting

strategies for engine failures during takeoff from offshore platforms, Aero. J. 99 (981) (1995) 15-25.

[16] W.M. Zhou, H. Wang, Research on inverse simulation's applications in teleoperation rendezvous and docking based on hyper-ellipsoidal restricted model predictive control for inverse simulation structure, P. I. Mech. Eng. G-J Aer. 229 (9) (2015) 1675-1689.

[17] R.A. Hess, Y. Zeyada, R. Heffley, Modeling and simulation for helicopter task analysis, J. Am. Helicopter. Soc. 47 (4) (2002) 243-252.

[18] S. Doyle, D.G. Thomson, Modification of a helicopter inverse simulation to include an enhanced rotor model, AIAA J. Aircraft. 37 (3) (2000) 536-538.

[19] M. Borri, C.L. Bottasso, F. Montelaghi, Numerical approach to inverse flight dynamics, J. Guid. Control. Dyn. 20 (4) (1997) 742-747.

[20] G. Avanzini, D.G. Thomson, Model predictive control architecture for rotorcraft inverse simulation, J. Guid. Control. Dyn. 36 (1) (2013) 207-217.

[21] D. Mayne, J. Rawlings, C. Rao, et al., Constrained model predictive control: stability and optimality, Automatica. 36 (6) (2000) 789-814.

[22] B.S. Crawford, Configuration design and efficient operation of redundant multi-jet systems, AIAA Guidance, Control, and Flight Mechanics Conference, Princeton, New Jersey, 1969.

[23] W.H. Tae, C.S Park, M.J. Tahk, H. Bang, Upper-stage launch vehicle servo controller design considering optimal thruster configuration, AIAA Guidance, Navigation, and Control Conference and Exhibit, Austin, Texas, 5330 (2003) 1-8.

[24] M. Wang, Y.C. Xie, A performance index for control capability of complex thruster configurations and its application, Aero. Control. App. 36 (2010) 36-41.

[25] A. Finn, S.F. Wu, A. Alexander, et al., On optimization of spacecraft thruster management function, AIAA Guidance, Navigation, and Control Conference and Exhibit, Providence, Rhode Island, 5133 (2004) 1-11.

[26] B.D. David, J.G. Brian, D.N. Anhtuan, Control allocation of reaction control jets and aerodynamic surfaces for entry vehicles, AIAA Guidance, Navigation and Control Conference and Exhibit, Hilton Head, South Carolina，6778 (2007) 1-24.

[27] M. Wang, Y.C. Xie, Spacecraft thrusters real time command allocation algorithm in consideration of thrust upper bounds and thruster failures, J. Astronaut. 31 (6) (2010) 1540-1546.

[28] A. S. Pablo, Control allocation for gimballed/fixed thrusters, Acta. Astronaut. 66 (2010) 587-594.

[29] S. Ricardo, A. Roberto, A.A. Pablo, Robust optimal solution to the

attitude/force control problem, IEEE Trans. Aero. Elec. Sys. 36 (3) (2000) 785-791.

[30] P. J. Wiktor, Minimum control authority plot: a tool for designing thruster systems, J. Guid. Control. Dyn. 17 (5) (1994) 998-1006.

[31] J.Y. Zhou, Research on teleoperation rendezvous and docking conception and critical technology, National University of Defense Technology, Chang Sha, 2013.

[32] W.M. Zhou, H. Wang, G.J. Tang, et al., Inverse simulation system for manual-controlled rendezvous and docking based on artificial neural network. Adv. Space. Res. 58 (2016) 938-949.

[33] W.M. Zhou, H. Wang, D.G. Thomson, et al., Inverse simulation system for evaluating qualities during rendezvous and docking. Acta. Astronaut. 137 (2017) 461-471.

[34] R. Isermann, Mechatronic systems-fundamentals, Springer, London, 2003.

[35] R. Isermann, Fault-diagnosis systems: an introduction from fault detection to fault tolerance, Springer, Berlin Heidelberg, 2006.

[36] M. Nicholas, D.M. Josue and J.W. Gloria, A new method of guidance control for autonomous rendezvous in a cluttered space environment, In: AIAA Guidance, Navigation and Control Conference and Exhibit, Hilton Head, South Carolina, 2007.

[37] K. Yamanake, K. Yokota, Guidance and navigation system design of r-bar approach for rendezvous and docking, In: 17th AIAA International Communications Satellite Systems Conference and Exhibit, Yokohama, Japan, 1998.

[38] Y.Z. Luo, L.B. Liang, H. Wang, et al., Quantitative performance for spacecraft rendezvous trajectory safety, J. Guid. Control. Dyn. 34 (4) (2011) 1264-1269.

[39] X.S. Wang, D.W. Wang, S.Q. Zhu, et al., Fractional Describing Function Analysis of PWPF Modulator,

Appendix A. Attitude Control Scheme

The attitude is controlled by the automatic control strategy. The method is illustrated as below.

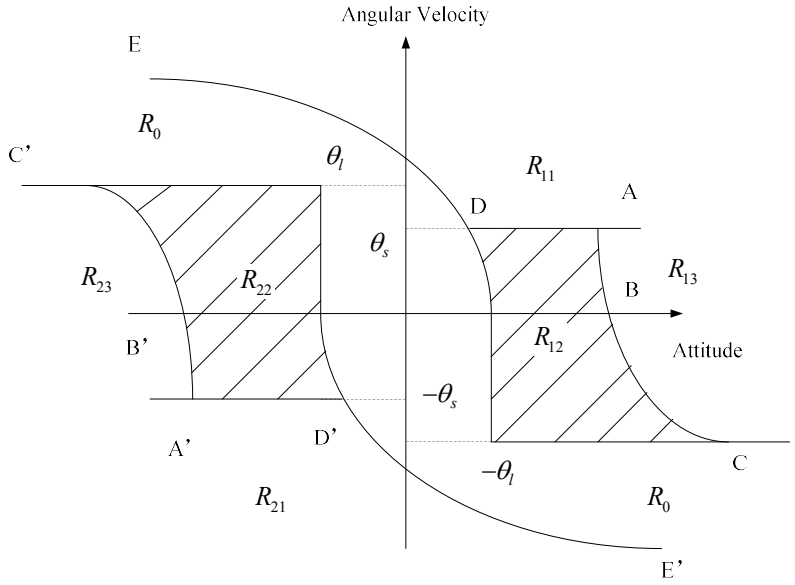

Fig. 1. Diagram of phase plane control.

The attitude state is divided into several switching areas by the switching lines. The switching lines are expressed as

Negative Opening Line DE: $\dot{\theta}^2 = -2a_0(\theta - d)$

Negative Closing Line BC: $\dot{\theta}^2 = 2a_0(\theta - d + \delta)$

Positive Opening Line $D'E'$: $\dot{\theta}^2 = 2a_0(\theta - d)$

Positive Closing Line $B'C'$: $\dot{\theta}^2 = -2a_0(\theta - d + \delta)$

where a_0 is determined by the moment of the attitude control thrusters; d, δ are determined by the control precisions of attitude angles and angular velocities separately. The border parameters of the switching lines are $\pm\dot{\theta}_s$ and $\pm\dot{\theta}_l$. The opening time parameters are set as btc_1, btc_2, and btc_3. These parameters are related with the control ability of the thrusters. The details of the phase plane strategy are

listed in Table 1.

Table 1
Attitude phase plane control strategy.

No.	Control Area	Description	Opening Time	Instruction
1	R_{11}/R_{21}	Thruster Full Opening De-/Accelerate Area	$T = btc_3 \Delta T$	ΔT is the sampling period. btc_1, btc_2, btc_3 adjust the opening time of the control thrusters.
2	R_{12}/R_{22}	Thruster Step Control Area	$T = btc_2 \Delta T$	
3	R_{13}/R_{23}	Thruster Step Control De-/Accelerate Area	$T = btc_2 \Delta T$	
4	R_0	Thruster Closing Area	$T = btc_1 \Delta T$	

Appendix B. Thruster Active Model

The spacecraft actuators used to execute the attitude and orbit control are generally relay-type thrusters. This kind of thruster has fixed amplitude thrust with changeable working time. Pulse thrust and continuous thrust can both be equivalent to the variable opening time of the relay-type thrusters. Thus, the continuous thrusts should be discretized by the pulse width and pulse frequency (PWPF) [39]. Based on the theorem of impulse, PW can be expressed as

$$m\Delta v = u_{\max}\Delta\tau = u^{*}\tau \tag{1}$$

where m is the mass of the propellant, u_{max} refers to the maximum thrust, u^{*} refers to the outputs of IS, $\Delta\tau$ refers to the opening time in one step τ. The whole process in T duration is explained in Fig. 1 and can be expressed as

$$m\Delta v_{total} = m\Delta v_1 + m\Delta v_2 + \ldots + m\Delta v_{N-1} + m\Delta v_N = m\int_0^T a(t)dt \tag{2}$$

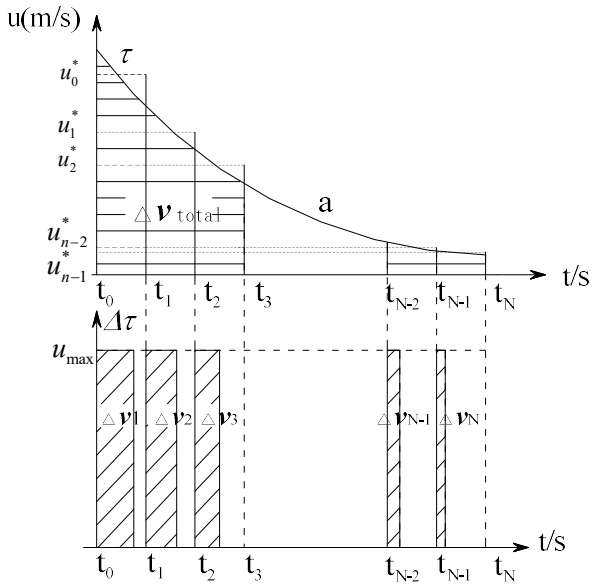

Fig. 1. PWPF of fixed amplitude thrust.

When the opening time $\Delta\tau$ is less than a certain value, the required correction is small which means the system cannot perceive this small error between the current

state and expected state and no operations happen. Using the sensitivity factor, the discrete process can represent the physical meaning naturally, which is given by

$$\Delta\tau = \begin{cases} 0, \Delta\tau \le k_t\tau \\ \Delta\tau, \Delta\tau > k_t\tau \end{cases} \tag{3}$$

$$|u| = \begin{cases} 0, & |u| \le k_f u_{\max} \\ u_{\max}, & |u| > k_f u_{\max} \end{cases} \tag{4}$$

where k_t refers to time sensitivity factor and k_f refers to acceleration sensitivity factor. Both factors represent for the sensitivity degree of the system to the offsets. According to Eq. (1), the sensitivity factor of the system should be $k = \min [k_t, k_f]$. The discrete results of IS can then be attained through Eq.(1) to Eq.(4).

The sensitivity factor represents the sensitivity degree of RVD IS system to the offsets between the desired and current states. The system with a smaller factor can react more quickly to the offset, the bigger factor on the contrary means less sensitivity. A manually controlled system has the same characteristics, i.e. the more sensitive the operators are, the stronger the perception ability of the system will be. The regulations both have some similarities, thus, the factors can also seem as the reflection of the operator's sensitivity regarding the results.